Enhancing Stability of DC Cascaded Systems With CPLs Using MPC Combined With NI and Accounting for Parameter Uncertainties

Hongjian Lin, *Senior Member, IEEE*, Henry Shu-Hung Chung, *Fellow, IEEE*, Ruihua Shen, *Member, IEEE*, and Yangxiao Xiang, *Member, IEEE*

***Abstract*—Compared with the traditional passive- and active-damping techniques for mitigating the impedance mismatch between the input impedance of constant power loads (CPLs) and the output impedance of the dc link within dc microgrids, there is a growing interest in leveraging model predictive control (MPC). MPC is proven to have the advantage of addressing the impedance mismatch issue, which leads to system instability and oscillations, owing to its constant handling, multivariable control, predictive capabilities, and optimization-based control. Nevertheless, the generalized MPC faces some technical challenges as it involves intricate enumeration and operations in switching state selection and observer design, thereby increasing computational complexity. Moreover, issues such as variable switching frequency and a lack of protection mechanisms impede its widespread application. To overcome these challenges, this article proposes an MPC technique employing a nonlinear inductor (NI) in the dc cascaded system to enable its faster and more stable transitions. The proposed controller utilizes the dead-beat principle to simplify the predictive process and alleviate the digital implementation burden in the control stage. The incorporation of the NI extends the stability range of the control-to-output transfer characteristics of the power conversion stage with CPL. Subsequently, two Luenberger observers are introduced, capable of handling load uncertainty and adapting to changes in system parameters. The selection criteria and stability analysis of the observer parameters are discussed. The proposed MPC is simple to implement and operates at a fixed switching frequency. Validation through simulation and experimental results confirms the effectiveness of the technique in improving system stability.**

***Index Terms*—Constant power load (CPL), dc cascaded system, model predictive control (MPC), nonlinear inductor (NI), parameter uncertainties, stability improvement.**

Manuscript received 17 May 2023; revised 30 September 2023 and 8 December 2023; accepted 23 January 2024. Date of publication 29 January 2024; date of current version 20 March 2024. This work was supported by the Research Grants Council of the Hong Kong Special Administration Region, China, under Grant CityU 11219722 and Grant CityU 11206620. Recommended for publication by Associate Editor J. Liu. *(Corresponding author: Yangxiao Xiang.)*

Hongjian Lin, Henry Shu-Hung Chung, and Yangxiao Xiang are with the Department of Electrical Engineering and the Centre for Smart Energy Conversion and Utilization Research, City University of Hong Kong, Hong Kong (e-mail: hongjian_lin@ieee.org; eeshc@cityu.edu.hk; yaxiang@cityu.edu.hk).

Ruihua Shen is with BYD Company Ltd., Shenzhen 518000, China (e-mail: rhshen2-c@my.cityu.edu.hk).

Color versions of one or more figures in this article are available at https://doi.org/10.1109/TPEL.2024.3359672.

Digital Object Identifier 10.1109/TPEL.2024.3359672

I. Introduction

ADVANCES in renewable energy resources like solar power and wind power, along with energy storage equipment, have driven the adoption of dc cascaded systems in dc microgrids (see Fig. 1) [1], [2], [3]. The main components of a dc cascaded system contain a source converter and a load converter [4]. The load converter, known as the constant power load (CPL), has a negative incremental input impedance or negative damping [5], which can result in an impedance mismatch with the output impedance of the source converter. This mismatch adversely impacts the power quality of the dc cascaded system, potentially leading to oscillation or even output collapse [6], [7]. Thus, addressing the instability issue in the dc cascaded system is important.

Two commonly employed approaches for enhancing the stability of dc cascaded systems with CPLs are passive damping and active damping, as reported in [8] and [9]. Passive damping techniques involve the incorporation of resistors, capacitors, and inductors in either parallel or series configuration between the source converter and the load converter. These techniques offer simplicity and eliminate the need for sophisticated control. However, the utilization of passive damping methods results in increased power dissipation and costs. In addition, for effective compensation of the negative damping characteristics of the CPL [10], [11], it is necessary to employ sufficiently large values for the parallel R and series LC damping. The series LC damping technique has been proven to be effective only when the equivalent impedance R_{CPL} is larger than $\sqrt{3L/2C}$ [10], [12].

Active damping is widely adopted to mitigate instability issues. To enhance system stability, a compensation current injection device was introduced in [13]. However, similar to passive damping techniques, the incorporation of extra devices introduces extra costs. To address these drawbacks, virtual impedance techniques, as proposed in [8], [14], [15], [16], [17], and [18], have been integrated into the modified control loop to achieve an active damping effect akin to passive damping techniques. These virtual impedances can be realized in either the source-side converter or the load-side converter. In the case of the load-side converter, extra feedforward active damping control is used to eliminate negative impedance and match the output impedance of the source converter, as discussed in

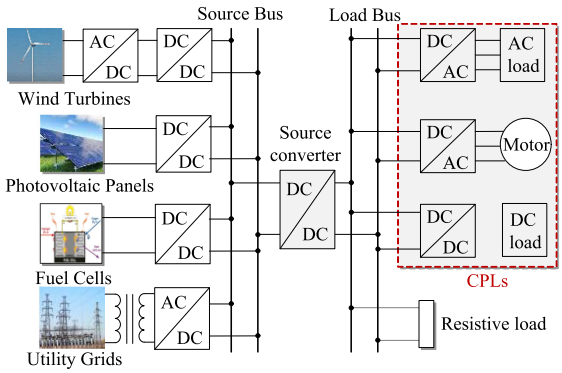

Fig. 1. General structure of a DC microgrid with power electronics devices.

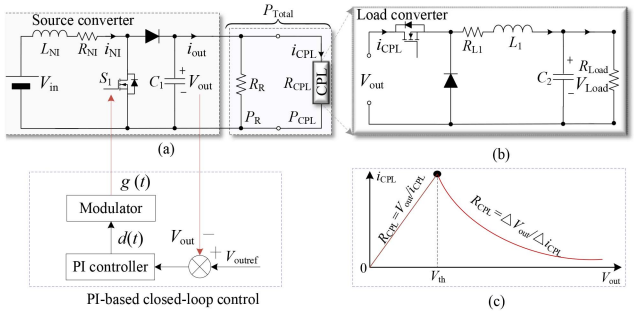

Fig. 2. Illustration of a DC cascaded system. (a) Boost converter with a resistive load and a CPL. (b) CPL. (c) Negative impedance characteristics.

[13], [14], and [15]. Particularly, Chen et al. propose a concise virtual impedance control strategy for CPLs, which has strong load power adaptability and less negative impact on dynamic performance. Conversely, the active damping approach in [8], [16], [17], and [18] utilizes feedback to superimpose the reference voltage, wherein the actual output voltage is controlled to track the new target reference voltage, which dynamically varies based on the output current. Thus, the active damping technique performs a similar function as the passive damping technique.

Although active damping techniques have gained significant interest and popularity due to their straightforward structures and effective outcomes, applying these techniques to nonlinear power converters poses challenges due to their inherent linear design. System oscillation tends to result in wider power fluctuations, implying that the compensation capability of these techniques is confined. Furthermore, enabling active impedance within a wide power variation can sometimes lead to a drop in the output voltage [16].

Various nonlinear control techniques have been proposed. They include sliding mode control [19], feedback linearization [20], [21], and model predictive control (MPC) [22], [23], [24]. Sliding mode control designs sliding surfaces to generate the duty cycle for the output power of the source-side converter, ensuring stability requirements are met. Feedback linearization control incorporates an optimized feedback loop to compensate for the nonlinearity of the dc cascaded system, enhancing stability without the need for generalized proportional-integral (PI) controllers. However, these techniques typically focus on single objectives and lack flexibility in achieving multiple objectives to improve system performance. In contrast, MPC techniques utilize cost factors and weight factors to address multiple objectives such as fast current control, stable voltage control, and fixed switching frequency [25], [26]. Despite their effectiveness, the tuning of weight factor values remains a complex process.

This article proposes a novel approach to enhance the system stability of dc cascaded systems. The technique combines improved MPC controllers with the utilization of nonlinear inductors (NIs) in the power conversion stage (PCS). By incorporating NIs, the stability range of the control-to-output transfer characteristics of the PCS operating with CPL can be expanded. Meanwhile, MPC offers advantageous features such as constraint handling, multivariable control, adaptability to system variations, predictive capabilities, and optimization-based control. To address parameter uncertainty, the control system integrates two Luenberger observers, ensuring robustness against parameter changes. Furthermore, the approach takes into consideration fixed-frequency operation and over-current protection to safeguard system operation.

Section II presents a comprehensive overview and analytical expression for NIs. Section III conducts a comparative analysis between NIs and fixed-value inductors (FIs) to assess their impact on the control-to-output transfer characteristics of the PCS with CPLs, emphasizing the advantageous stability-enhancing attributes of NIs. The limitations of PI control techniques for the PCS with NIs are identified, prompting the introduction of MPC in Section IV. This section also encompasses the design considerations for the inner current loop, outer voltage loop, and observer. Section V presents the results of simulations and experiments, providing empirical evidence in support of the proposed method.

II. Overview of NI Characteristics

In Fig. 2(a), a dc cascaded system is depicted. The source converter is a boost converter, where the input voltage is denoted as $V_{\rm in}$ and the output voltage as $V_{\rm out}$. It draws an input current represented by $i_{\rm NI}$ and delivers an output current denoted as $i_{\rm out}$. It incorporates an output capacitor C_1. The load on the source converter comprises two types. The first type is a resistive load denoted as $R_{\rm R}$, while the second type is a CPL. The power consumed by $R_{\rm R}$ is represented as $P_{\rm R}$, and the power consumed by a CPL is denoted as $P_{\rm CPL}$. The current supplied to the CPL is $i_{\rm CPL}$. The CPL is practically a converter, which is named a load converter. It is illustrated in Fig. 2(b) using a buck converter configuration outputting a load voltage $V_{\rm load}$.

The most stringent operation is when $R_{\rm R} \to \infty$, that is, the load on the source converter is purely CPL. A mismatch between the output impedance of the source converter and the negative incremental impedance of the CPL can lead to system instability. The controller in the source converter needs to ensure system stability even when $R_{\rm R} \to \infty$. Fig. 2(c) shows the input impedance of the load converter. The load converter exhibits positive resistance when the input voltage is below $V_{\rm th}$. CPL property starts when the input voltage is above $V_{\rm th}$.

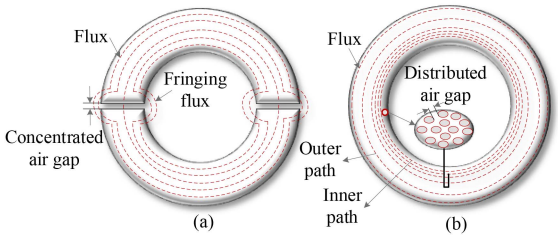

Fig. 3. Magnetic cores. (a) Ferrite core with concentrated air gaps for FI. (b) Powder core with distributed air gaps for NI.

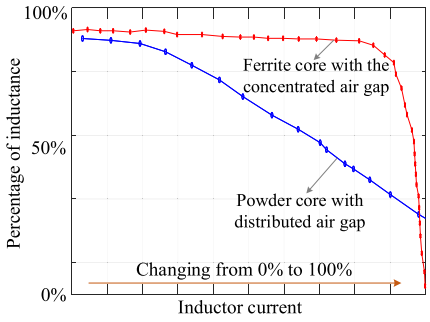

Fig. 4. Change of inductance versus inductor current.

Fig. 3 illustrates two types of magnetic cores [7]. The first one is a ferrite core with concentrated air gaps, commonly employed to implement FIs. In this design, the permeability of the core experiences a significant drop when the magnetic flux density exceeds the saturation point, leading to demagnetization. The purpose of incorporating air gaps is to prevent magnetic saturation and subsequent demagnetization. Consequently, if an inductor utilizes this type of core, its inductance will noticeably decrease when the current surpasses the saturation point.

The second core type is a powder core with distributed air gaps, typically utilized in the construction of NIs. In this configuration, the inner path length is shorter than the outer path length, resulting in a lower reluctance in the inner path. As the current through the NI increases, magnetic saturation begins in the inner path and gradually progresses to the outer path.

The soft saturation property will benefit the application due to its high reliability in enduring sudden overcurrent. Fig. 4 shows the change of inductance versus inductor current with the two types of magnetic cores. With respect to a given NI inductance, $L_{\rm NI}$ and $i_{\rm NI}$ are expressed as

$$\begin{cases} L_{\rm NI} = \dfrac{\mu S}{l} N_{\rm NI}^2 \\ I_{\rm NI} = \dfrac{F}{N_{\rm NI}} \end{cases} \tag{1}$$

where μ is the permeability of air, S is the coil cross-sectional area, l is coil length, F is the magnetomotive force, and $N_{\rm NI}$ is the number of turns of the winding.

For the sake of analysis, the estimated relationship between the inductance and current of NI is modeled by the following formula:

$$L_{\rm NI}(i_{\rm NI}) = \frac{L_{\rm NI\,min}}{1 + k i_{\rm NI}^2} \tag{2}$$

TABLE I
PARAMETERS USED IN THE ANALYSIS

C_1	$R_{\rm NI}$, $R_{\rm FI}$	$L_{\rm NImin}$, $L_{\rm FI}$	k	$V_{\rm in}$	$V_{\rm out}$	$R_{\rm R}$
200 μF	0.3 Ω	1.2 mH	0.2 A^{-2}	12 V	24 V	∞

where k defines the rate of change of $L_{\rm NI}$ with respect to $i_{\rm NI}$.

Based on the analysis of the NI characteristics, the soft saturation performance emerges as a key factor in contributing to the enhancement of system reliability. This is particularly evident as the inductance of the NI gradually decreases with the rise in dc current, as depicted by the analytical model in (2). Consequently, the subsequent step involves demonstrating the improved stability of the dc cascaded system through the utilization of the NI in the PCS.

III. IMPACT OF NIS ON IMPROVING STABILITY RANGE

In this section, the augmented stability of the dc cascaded system by integrating the NI is demonstrated. In addition, a comparative analysis to assess the impact of FIs and NIs on the control-to-output transfer characteristics of the PCS is conducted when a CPL is connected at the output. Based on Fig. 2, a continuous time-domain model can be expressed as [25], [26], [27]

$$\begin{cases} \dfrac{{\rm d}i_{\rm NI}}{{\rm d}t} = \dfrac{V_{\rm in} - i_{\rm NI}(t) R_{\rm NI}}{L_{\rm NI}} + [d(t) - 1]\dfrac{V_{\rm out}(t)}{L_{\rm NI}} \\ \dfrac{{\rm d}V_{\rm out}(t)}{{\rm d}t} = \dfrac{1 - d(t)}{C_1} i_{\rm NI}(t) - \dfrac{V_{\rm out}(t)}{C_1 R_{\rm R}} - \dfrac{P_{\rm CPL}(t)}{V_{\rm out} C_1} \end{cases} \tag{3}$$

where $d(t)$ is the duty cycle of the main switch of the source converter.

In the following analysis, the worst-case scenario with $R_{\rm R} \to \infty$ is considered. Based on (3), the state variables are perturbed around the equilibrium point with the quiescent duty cycle D. It can be shown that the Jacobian matrices $J_{\rm FI}$ and $J_{\rm NI}$ for FI and NI, respectively, are

$$J_{\rm FI} = \begin{bmatrix} -\dfrac{R_{\rm FI}}{L_{\rm FI}} & -\dfrac{1-D}{L_{\rm FI}} \\ \dfrac{1-D}{C_1} & \dfrac{P_{\rm CPL}}{C_1 V_{\rm out}^2} \end{bmatrix} \tag{4a}$$

$$J_{\rm NI} = \begin{bmatrix} -\dfrac{R_{\rm NI}}{L_{\rm NI}} & -\dfrac{1-D}{L_{\rm NI}} \\ \dfrac{1-D}{C_1} & \dfrac{P_{\rm CPL}}{C_1 V_{\rm out}^2} \end{bmatrix} \tag{4b}$$

where $L_{\rm FI}$ and $R_{\rm FI}$ are the inductance and resistance of the FI, respectively, and $L_{\rm NI}$ and $R_{\rm NI}$ are the inductance and resistance of the NI, respectively.

Based on the parameters given in Table I, Fig. 5 shows the trajectories of eigenvalues (λ) in relation to $P_{\rm CPL}$ with FI and NI, respectively. The results demonstrate that as $P_{\rm CPL}$ increases, the eigenvalues associated with the NI consistently remain in the left half plane. Conversely, with the FI, the eigenvalues may transition into the right half plane as the power of the CPL increases. These results indicate that utilization of the NI effectively broadens the stability range, delivering enhanced stability performance compared to the converter equipped with FI.

Building upon this inherent capability of the NI, Section IV presents the integration of the NI into the MPC controller of

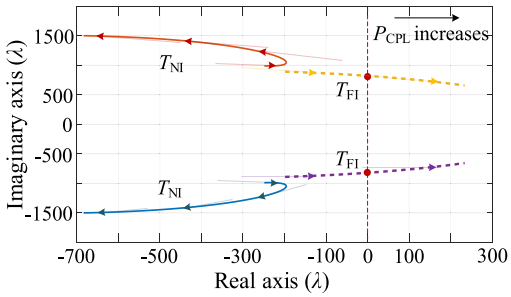

Fig. 5. Trajectories of the eigenvalues in relation to P_{CPL}. T_{NI}: Trajectories with NI. T_{FI}: Trajectories with FI.

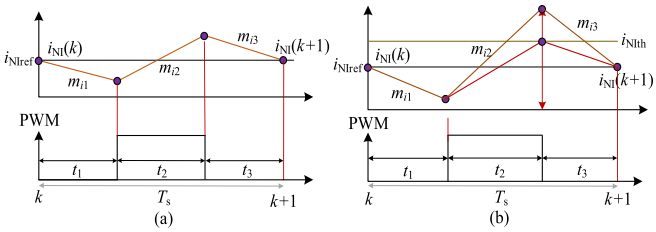

Fig. 6. Waveforms of the NI current and gate signal. (a) Without NI current limit. (b) With NI current limit.

the current loop to accomplish closed-loop control of the dc cascaded system.

IV. Proposed MPC Framework

As discussed hereinbefore, the generalized MPC controllers in [22] and [24] result in a complex computational burden due to the necessity for intricate arithmetic, enumeration, and optimized operations. Moreover, the inclusion of variable switching frequency and the absence of a protective function impede the progression of these techniques. Notably, these techniques only employ the FIs in the PCS, accordingly, the system stability range cannot be improved inherently. Consequently, this section will propose an improved MPC controller in the MPC framework. It concurrently integrates the NI from (2) into the current loop to simplify the digital implementation and expand the stability range.

Based on the aforementioned consideration and for the sake of realizing the dc cascaded system operation, the proposed MPC framework comprises the following three key components:

1) the current loop;
2) the voltage loop;
3) the observers.

The design details of each component are outlined below.

A. Design of the Current Loop

The source converter operates in continuous conduction mode. As illustrated in Fig. 6, each switching cycle is divided into three time intervals. They are t_1, t_2, and t_3. Within t_1 and t_3, the main switch S_1 is OFF. Within t_2, S_1 is ON. Equation (3) is discretized into the following set of difference equations by using the forward Euler method to predict the NI current and output voltage after one switching cycle:

$$\begin{cases} i_{\mathrm{NI}}(k+1)=(1-\frac{T_{\mathrm{s}}R_{\mathrm{NI}}}{L_{\mathrm{NI}}})i_{\mathrm{NI}}(k)+[d(k)-1]\frac{T_{\mathrm{s}}}{L_{\mathrm{NI}}}V_{\mathrm{out}}(k)+\frac{T_{\mathrm{s}}}{L_{\mathrm{NI}}}V_{\mathrm{in}} \\ V_{\mathrm{out}}(k+1)=\frac{T_{\mathrm{s}}}{C_1}i_{\mathrm{NI}}(k)+V_{\mathrm{out}}(k)-\frac{P_{\mathrm{CPL}}(k)T_{\mathrm{s}}}{C_1V_{\mathrm{out}}(k)}-\frac{T_{\mathrm{s}}}{C_1}i_{\mathrm{NI}}(k)d(k) \end{cases} \tag{5}$$

where T_{s} is the sampling period. It is the same as the switching period of S_1.

Equation (5) can be written in the form of

$$\begin{cases} \boldsymbol{X}(k+1)=\boldsymbol{A}\boldsymbol{X}(k)+\boldsymbol{B}d(k)+\boldsymbol{E}\boldsymbol{v} \\ \boldsymbol{Y}(k)=\boldsymbol{C}\boldsymbol{X}(k) \end{cases} \tag{6}$$

where

$$\boldsymbol{X}(k)=[i_{\mathrm{NI}}(k)\quad V_{\mathrm{out}}(k)]^T,$$

$$\boldsymbol{A}=\begin{bmatrix} 1-\frac{T_{\mathrm{s}}R_{\mathrm{NI}}}{L_{\mathrm{NI}}} & -\frac{T_{\mathrm{s}}}{L_{\mathrm{NI}}} \\ \frac{T_{\mathrm{s}}}{C_1} & 1-\frac{T_{\mathrm{s}}}{C_1R_{\mathrm{CPL}}} \end{bmatrix},$$

$$\boldsymbol{B}=\begin{bmatrix} \frac{T_{\mathrm{s}}}{L_{\mathrm{NI}}}V_{\mathrm{out}}(k) \\ -\frac{T_{\mathrm{s}}}{C_1}i_{\mathrm{NI}}(k) \end{bmatrix}$$

$$\boldsymbol{E}=\begin{bmatrix} \frac{T_{\mathrm{s}}}{L_{\mathrm{NI}}} \\ 0 \end{bmatrix},\ \boldsymbol{C}=\begin{bmatrix} 1 & 0 \end{bmatrix},\ \boldsymbol{v}=V_{\mathrm{in}}.$$

As shown in Fig. 6(a), the rate of change of the NI current is assumed to be constant within each time interval. Based on (5) and (6), we obtained

$$\begin{cases} m_{i1}=\frac{V_{\mathrm{in}}-i_{\mathrm{NI}}(k)-V_{\mathrm{out}}(k)}{L_{\mathrm{NI}}} \\ m_{i2}=\frac{V_{\mathrm{in}}-i_{\mathrm{NI}}(k)R_{\mathrm{NI}}}{L_{\mathrm{NI}}} \\ m_{i3}=\frac{V_{\mathrm{in}}-i_{\mathrm{NI}}(k)-V_{\mathrm{out}}(k)}{L_{\mathrm{NI}}} \end{cases} \tag{7}$$

where m_{i1}, m_{i2}, and m_{i3} are the slopes within the time intervals of t_1, t_2, and t_3, respectively.

Subsequently, based on Figs. 6(a) and (7), $i_{\mathrm{NI}}(k+1)$ can be expressed as

$$i_{\mathrm{NI}}(k+1)=i_{\mathrm{NI}}(k)+m_{i1}t_1+m_{i2}t_2+m_{i3}t_3. \tag{8}$$

Assume that $t_1=t_3$. The modulation is centre-aligned. Thus

$$\begin{cases} t_2=d(k)T_{\mathrm{s}} \\ t_1=[1-d(k)]T_{\mathrm{s}}/2 \\ t_3=[1-d(k)]T_{\mathrm{s}}/2. \end{cases} \tag{9}$$

By substituting (9) and (7) into (8), we obtained

$$i_{\mathrm{NI}}(k+1)=(1-\frac{R_{\mathrm{NI}}T_{\mathrm{s}}}{L_{\mathrm{NI}}})i_{\mathrm{NI}}(k) + \frac{V_{\mathrm{in}}-[1-d(k)]V_{\mathrm{out}}(k)}{L_{\mathrm{NI}}}T_{\mathrm{s}}. \tag{10}$$

Based on the dead-beat principle and the optimal control principle [28], [29], [30], $i_{\mathrm{NI}}(k+1)=i_{\mathrm{NIref}}$, and hence

$$d(k)=1-\frac{[i_{\mathrm{NI}}(k)-i_{\mathrm{NIref}}]L_{\mathrm{NI}}+[V_{\mathrm{in}}-i_{\mathrm{NI}}(k)R_{\mathrm{NI}}]T_{\mathrm{s}}}{V_{\mathrm{out}}(k)T_{\mathrm{s}}}. \tag{11}$$

To limit the amplitude of i_{NI}, the proposed MPC technique predicts the rate of change of i_{NI} and ensures that the predicted value of the NI current after one switching cycle does not exceed

the limit i_{NIth}. Consequently, as shown in Fig. 6(b), the sum of $i_{\mathrm{NI}}(k)$ and the terms $m_{i1}t_1$ and $m_{i2}t_2$ must be less than i_{NIth}. Thus

$$i_{\mathrm{NIth}} \geq i_{\mathrm{NI}}(k) + T_{\mathrm{s}}\left[\left(\frac{V_{\mathrm{in}} - R_{\mathrm{NI}}i_{\mathrm{NI}}}{L_{\mathrm{NI}}}\right)\left(\frac{1+d(k)}{2}\right) - \frac{V_{\mathrm{out}}(k)(1-d(k))}{2}\right]. \tag{12}$$

Since the proposed MPC technique utilizes the predicted NI current as the target current, the duty cycle d_{th} is

$$d_{\mathrm{th}}(k) = \frac{2L_{\mathrm{NI}}[i_{\mathrm{NIth}} - i_{\mathrm{NI}}(k)] - T_{\mathrm{s}}[(V_{\mathrm{in}} - R_{\mathrm{NI}}i_{\mathrm{NI}}) - V_{\mathrm{out}}]}{T_{\mathrm{s}}[(V_{\mathrm{in}} - R_{\mathrm{NI}}i_{\mathrm{NI}}) + V_{\mathrm{out}}]}. \tag{13}$$

Without loss of generality, i_{NIth} can be set to be equal to $i_{\mathrm{NIref.}}$ Both the duty cycles, $d(k)$ and $d_{\mathrm{th}}(k)$, are calculated using i_{NIref} and i_{NIth}, respectively, as per (11) and (13). Hence it is nontrivial to obtain i_{NIref}. The following section outlines how i_{NIref} is derived.

B. Design of Voltage Loop

The PI controller shown in Fig. 2(a) forms the basis of the generalized closed voltage loop. The difference between the actual and target NI currents is fed into the PI controller to calculate the duty cycle $d(t)$ for S_1. However, according to [9] and the discussion in Section III, the integrator of the PI controller decreases the phase margin, ultimately reducing the stable range of the dc cascaded system. An alternative controller is proposed. Let P_{in} be the active power of the dc source voltage. P_{NI} is the power loss of the NI. Under the steady state operation

$$P_{\mathrm{in}} = P_{\mathrm{CPL}} + P_{\mathrm{NI}} \Rightarrow V_{\mathrm{in}}I_{\mathrm{NIref}} = P_{\mathrm{CPL}} + I_{\mathrm{NIref}}^2 R_{\mathrm{NI}} \tag{14}$$

where I_{NIref} refers to the effective value of i_{NIref} and R_{CPL} represents the equivalent input resistance of the CPL.

Based on (14), I_{NIref} is calculated by

$$I_{\mathrm{NIref}} = \frac{V_{\mathrm{in}}}{2R_{\mathrm{NI}}} - \sqrt{\frac{V_{\mathrm{in}}^2}{4R_{\mathrm{NI}}^2} - \frac{P_{\mathrm{CPL}}}{R_{\mathrm{NI}}}}. \tag{15}$$

Let the ripple around I_{NIref} be $\hat{i}_{\mathrm{NIref}}$, which is calculated by $G_{\mathrm{P}}[V_{\mathrm{outref}} - V_{\mathrm{out}}]$, where G_{p} is the gain to amplify the difference between V_{out} and V_{outref}. The approximated instantaneous target value of the NI current, i.e., i_{NIref}, is

$$\begin{aligned} i_{\mathrm{NIref}} &= I_{\mathrm{NIref}} + \hat{i}_{\mathrm{NIref}} \\ &= \frac{V_{\mathrm{NI}}}{2R_{\mathrm{NI}}} - \sqrt{\frac{V_{\mathrm{NI}}^2}{4R_{\mathrm{NI}}^2} - \frac{P_{\mathrm{CPL}}}{R_{\mathrm{NI}}}} + G_{\mathrm{P}}[V_{\mathrm{outref}} - V_{\mathrm{out}}]. \end{aligned} \tag{16}$$

To improve system phase margin and stability, the outer voltage loop utilizes a model in (16), which excludes the integrator. This approach offers advantages compared to the traditional PI-based control.

Once the inner current and outer voltage loops are designed, it becomes essential to observe and analyze the system parameters to enhance its robustness.

C. Design of Observers

This section designs observers to evaluate uncertain and unknown parameters within the dc cascaded system. While the generalized MPC techniques in [22] and [24] utilize nonlinear disturbance observers and sliding mode observers (SMOs) to estimate these parameters. Nonlinear disturbance observers (NDOs) and SMOs involve complex arithmetic operations, including high-order operations, which escalates the digital implementation burden. Furthermore, the SMOs are susceptible to instability when introduced to larger signals, resulting in undesigned shaking [31], [32]. Therefore, Luenberger observers are introduced in this section for the system parameter estimation, ensuring a simple control structure, fast dynamic response, and high estimation precision, as compared to SMOs [33].

Regarding the duty cycles determined by (11) and (13), they are dependent on parameters such as the source voltage and NI resistance. As these parameters vary with operating conditions, such as temperature, during operation, the system stability and robustness can be negatively affected. It is crucial to devise a solution to conduct online observation of these parameters. Building upon the merits of the Luenberger observer described hereinbefore, two Luenberger observers are designed. The first one is used to estimate the source voltage and the NI resistance, whereas the second one is used to estimate P_{CPL}.

1) Observer 1 for Source Voltage and NI Resistance: From (5), we get

$$\frac{\mathrm{d}i_{\mathrm{NI}}}{\mathrm{d}t} = \underbrace{\frac{V_{\mathrm{in}} - R_{\mathrm{NI}}i_{\mathrm{NI}}}{L_{\mathrm{NI}}}}_{\text{The first term}} + \underbrace{[d_{\mathrm{opt}}(t) - 1]\frac{V_{\mathrm{out}}(t)}{L_{\mathrm{NI}}}}_{\text{The second term}} \tag{17}$$

where $d_{\mathrm{opt}}(t)$ is the duty cycle corresponding to (11) or (13). If (11) is satisfied, $d_{\mathrm{opt}}(t) = d(t)$. Otherwise, $d_{\mathrm{opt}}(t) = d_{\mathrm{th}}(t)$.

Equation (17) comprises two terms, with the first term including V_{in} and R_{NI}. Thus, it is necessary to define

$$w(t) = \frac{V_{\mathrm{in}} - i_{\mathrm{NI}}(t)R_{\mathrm{NI}}}{L_{\mathrm{NI}}}. \tag{18}$$

Thus

$$\begin{cases} i_{\mathrm{NI}}(k+1) = i_{\mathrm{NI}}(k) + w(k)T_{\mathrm{s}} + \frac{[d_{\mathrm{opt}}(k)-1]V_{\mathrm{out}}(k)T_{\mathrm{s}}}{L_{\mathrm{NI}}} \\ w(k+1) = w(k). \end{cases} \tag{19}$$

In matrix form

$$\begin{cases} \boldsymbol{X}_1(k+1) = \boldsymbol{A}_1\boldsymbol{X}_1(k) + \boldsymbol{B}_1[1 - d_{\mathrm{opt}}(k)] \\ \boldsymbol{Y}_1(k) = \boldsymbol{C}_{11}\boldsymbol{X}_1(k+1) \end{cases} \tag{20}$$

where $\boldsymbol{X}(k) = [i_{\mathrm{NI}}(k) \quad w(k)]^T$, $\boldsymbol{A}_1 = \begin{bmatrix} 1 & T_{\mathrm{s}} \\ 0 & 1 \end{bmatrix}$, $\boldsymbol{B}_1 = \begin{bmatrix} \frac{T_{\mathrm{s}}}{L_{\mathrm{NI}}}V_{\mathrm{out}}(k) \\ 0 \end{bmatrix}$ $\boldsymbol{X}(k) = \begin{bmatrix} \frac{-V_{\mathrm{out}}(k)}{L_{\mathrm{NI}}}T_{\mathrm{s}} & 0 \end{bmatrix}^T$, and $\boldsymbol{C}_{11} = [1 \quad 0]$.

Based on (20), a Luenberger observer is designed as

$$\begin{cases} \boldsymbol{X}_1(\tilde{k}+1) = \boldsymbol{A}_1\boldsymbol{X}_1(\tilde{k}) + \boldsymbol{B}_1[1 - d_{\mathrm{opt}}(k)] \\ +\boldsymbol{O}[Y_1(k) - Y_1(\tilde{k})] \\ \boldsymbol{Y}_1(\tilde{k}+1) = \boldsymbol{C}_{11}\boldsymbol{X}_1(\tilde{k}+1) \end{cases} \tag{21}$$

where $\boldsymbol{X}(k) = [i_{\mathrm{NI}}(\tilde{k}) \quad w(\tilde{k})]^T$ and $\boldsymbol{O} = [O_1 \quad O_2]^T$. Matrix $\boldsymbol{O}$ is the observer parameters for V_{in} and R_{NI}.

According to (21)

$$\begin{cases} w(\tilde{k}+1) = w(\tilde{k}) + O_1[i_{\rm NI}(k) - i_{\rm NI}(\tilde{k})] \\ \tilde{i}_{\rm NI}(k+1) = \tilde{i}_{\rm NI}(k) + O_2[i_{\rm NI}(k) - i_{\rm NI}(\tilde{k})] \\ \quad + T_{\rm s}[w(\tilde{k}) - \frac{[1-d_{\rm opt}(k)]V_{\rm out}(k)}{L_{\rm NI}}. \end{cases} \tag{22}$$

Then, (11) and (13) can be written as

$$\begin{cases} d(k) = 1 - \frac{[i_{\rm NI}(k)-i_{\rm NIref}]L_{\rm NI}+w(\tilde{k})T_{\rm s}L_{\rm NI}}{V_{\rm out}(k)T_{\rm s}} \\ d_{\rm th}(k) = \frac{2L_{\rm NI}[i_{\rm NIth}-i_{\rm NI}]L_{\rm NI}-w(\tilde{k})T_{\rm s}L_{\rm NI}+V_{\rm out}T_{\rm s}}{V_{\rm out}(k)T_{\rm s}+L_{\rm NI}w(\tilde{k})T_{\rm s}}. \end{cases} \tag{23}$$

Hence, the duty cycles $d(k)$ and $d_{\rm th}(k)$ become insusceptible to the variations of the source voltage and the NI resistance.

2) Observer 2 for P_{CPL}*:* Based on (5), the derivative of the output voltage is

$$\frac{{\rm d}V_{\rm out}}{{\rm d}t} = [1 - d_{\rm opt}(t)]\frac{i_{\rm NI}}{C_1} - \frac{i_{\rm out}}{C_1}. \tag{24}$$

Equation (24) is discretized by the forward Euler method to give

$$V_{\rm out}(k+1) - V_{\rm out}(k) = -T_{\rm s}[d_{\rm opt}(k) - 1]\frac{i_{\rm NI}(k)}{C_1} - \frac{i_{\rm out}(k)}{C_1}. \tag{25}$$

A state-space mathematical model can thus be derived as

$$\begin{cases} \boldsymbol{X}_2(k+1) = \boldsymbol{A}_2\boldsymbol{X}_2(k) + \boldsymbol{B}_2[1 - d_{\rm opt}(k)] \\ \boldsymbol{Y}_2(k+1) = \boldsymbol{C}_{22}\boldsymbol{X}_2(k+1) \end{cases} \tag{26}$$

where $\boldsymbol{X}_2(k) = [i_{\rm out}(k) \quad V_{\rm out}(k)]^T$, $\boldsymbol{A}_2 = \begin{bmatrix} 1 & 0 \\ T_{\rm s}/C_1 & 1 \end{bmatrix}$, $\boldsymbol{B}_2 = [0 \quad T_{\rm s}i_{\rm NI}(k)/C_1]^T$, and $\boldsymbol{C}_{22} = [0 \quad 1]$.

To construct an observer for $P_{\rm CPL}$, (26) is expressed as

$$\begin{cases} \boldsymbol{X}_2(\tilde{k}+1) = \boldsymbol{A}_2\boldsymbol{X}_2(\tilde{k}) + \boldsymbol{B}_2[1 - d_{\rm opt}(k)] \\ \quad + \boldsymbol{P}[Y_2(k) - Y_2(\tilde{k})] \\ \boldsymbol{Y}_2(\tilde{k}+1) = \boldsymbol{C}_{22}\boldsymbol{X}_2(\tilde{k}+1) \end{cases} \tag{27}$$

where $\boldsymbol{X}_2(k) = [i_{\rm out}(\tilde{k}) \quad V_{\rm out}(\tilde{k})]^T$ and $\boldsymbol{P} = [p_1 \quad p_2]^T$. Matrix $\boldsymbol{P}$ contains the observer parameters for $P_{\rm CPL}$.

From (23), we get

$$P_{\rm CPL}(\tilde{k}+1) = V_{\rm out}(\tilde{k}+1).i_{\rm out}(\tilde{k}+1). \tag{28}$$

The relationships among the actual variables, estimated variables, and observer parameters can be found in (21) and (27).

D. Design of Observer Parameters and Stability Analysis

From (20), (21), (26), and (27), we get

$$\begin{cases} \boldsymbol{X}_1(k+1) - \boldsymbol{X}_1(\tilde{k}+1) = (\boldsymbol{A}_1 - \boldsymbol{OC_{11}})[\boldsymbol{X}_1(k) - \boldsymbol{X}_1(\tilde{k})] \\ \boldsymbol{X}_2(k+1) - \boldsymbol{X}_2(\tilde{k}+1) = (\boldsymbol{A}_2 - \boldsymbol{PC}_{22})[\boldsymbol{X}_2(k) - \boldsymbol{X}_2(\tilde{k})]. \end{cases} \tag{29}$$

Based on (29), for stable operation, it is essential that the matrices ($\boldsymbol{A_1}$-$\boldsymbol{OC_{11}}$) and ($\boldsymbol{A_2}$-$\boldsymbol{PC_{22}}$) consist of only real numbers to construct Hurwitz matrices. Specifically, the absolute values of the eigenvalues for these matrices must be less than 1. That is

$$\begin{cases} \left|1 - 0.5O_1 - 0.5\sqrt{O_1^2 + 4T_s - 4O_2T_s}\right| < 1 \\ \left|0.5(2 - O_1 + \sqrt{O_1^2 + (4 - 4O_2)T_s}\right| < 1 \end{cases} \tag{30}$$

$$\begin{cases} \left|1 - 0.5p_2 - \frac{0.5\sqrt{Cp_2^2+4p_1T_{\rm s}}}{\sqrt{C_1}}\right| < 1 \\ \left|1 - 0.5p_2 + \frac{0.5\sqrt{Cp_2^2+4p_1T_{\rm s}}}{\sqrt{C_1}}\right| < 1. \end{cases} \tag{31}$$

1) Design of Observer Parameters: To precisely quantify the observer parameters, it is crucial to design the system such that all eigenvalues are within the unit circle. Based on (21) and (27), the control loops, which contain parameters O_2 and p_1, respectively, exhibit faster dynamic response and higher bandwidths. It is prioritized to tune O_2 and p_1 while keeping O_1 and p_2 fixed. Accordingly, the parameters for observers 1 and 2 are interpreted as follows.

1) With $-0.5 < O_1 < 0.5$ and $-0.5 < O_2 < 0.5$, the eigenvalues are placed, as shown in Fig. 7(a). Some eigenvalues are outside the unit circle. However, if the range is confined to $O_1 = 0.5$ and $-0.5 < O_2 < 0.5$, all eigenvalues will be inside the unit circle [see Fig. 7(b)], which implies that for stabilizing observer 1, O_1 parameters are set by this range.
2) To ensure the stable functioning of observer 2, the initialization of $-0.5 < p_1 < 0.5$ and $-0.5 < p_2 < 0.5$ are assumed as well. However, as illustrated in Fig. 7(c), this set of parameters results in a few eigenvalues located outside the unit circle. To mitigate this phenomenon, the parameter set of $-0.5 < p_1 < 0.5$ and $p_2 = 0.5$ is utilized, which brings most of the eigenvalues within the unit circle, as can be observed from Fig. 7(d). Furthermore, if the parameters are set to $-0.5 < p_1 < 0$ and $p_2 = 0.5$, all eigenvalues will be located inside the unit circle, as shown in Fig. 7(e). Hence, to ensure the stable operation of observer 2, $p_2 = 0.5$ and $-0.5 < p_1 < 0$.
3) To account for the impact of $L_{\rm NI}$ and C_1, since $L_{\rm NI}$ is removed from the parameter matrix ($\boldsymbol{A_1}$-$\boldsymbol{OC_{11}}$), variation of $L_{\rm NI}$ does not affect the observer stability. In terms of the output capacitance C_1, on account of the value of C_1 existing in ($\boldsymbol{A_2}$-$\boldsymbol{PC_{22}}$), it is crucial to discuss the impact of C_1.

Initially, the observer parameters are set within the allowable range, i.e., $O_1 = 0.5$, $O_2 = 0.2$, $p_1 = -0.2$, and $p_2 = 0.5$. As depicted in Fig. 7(f), when the variation of the output capacitance C_1, i.e., $\triangle C_1$ is within the range of $\pm 20\% C_1$, the system remains stable, which indicates that the appropriate observer parameters enhance the system robustness.

2) Stability Analysis: According to (5), (16), (21), (27), and (29), the system average state-space model represented as (32) is derived. Based on this model, the location of eigenvalues of matrices, as the control parameter $G_{\rm p}$ in (16) varies, is investigated, meanwhile operating under a practical scenario where the values of $L_{\rm NI}$ and $R_{\rm NI}$ undergo $\pm 20\%$ variation within the acceptable tolerances. In addition, the observer parameters O_1, O_2, p_1, and p_2 are determined by (29) to (31) and are kept constant in the study.

Fig. 8(a)–(c) shows the results when $G_{\rm p}$ equals 2, 6, and 10, respectively. When $G_{\rm p}$ equals 2 or 6, all eigenvalues lie in the unit circle even if $L_{\rm NI}$ and $R_{\rm NI}$ undergo $\pm 20\%$ variation. In general, with a larger value of $G_{\rm p}$ more than 10, the poles will be closer

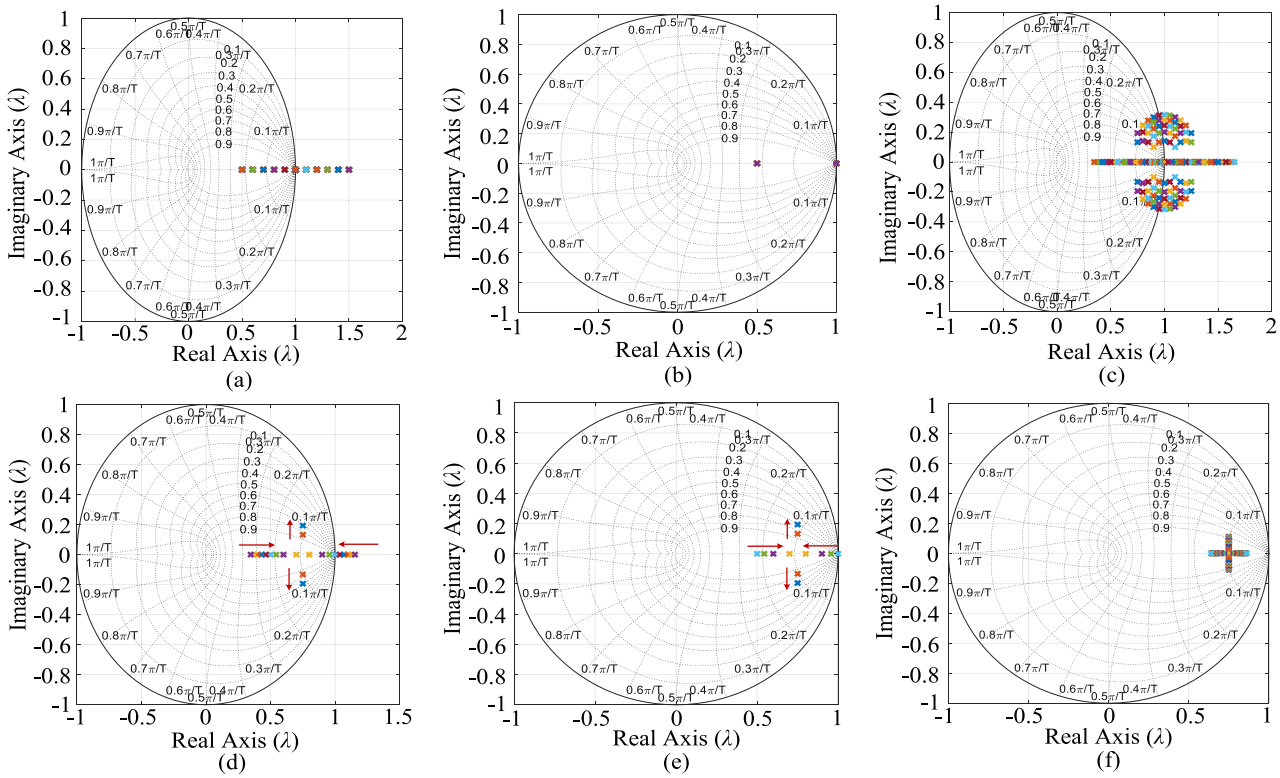

Fig. 7. Trajectories of eigenvalues. (a) $-0.5<O_1<0.5$, $-0.5<O_2<0.5$. (b) $-0.5<O_2<0.5$, $O_1 = 0.5$. (c) $-0.5<p_1<0.5$, $-0.5<p_2<0.5$. (d) $-0.5<p_1<0.5$, $p_2 = 0.5$. (e) $-0.5<p_1<0$, $p_2 = 0.5$. (f) $\triangle C_1 = \pm 20\% C_1$.

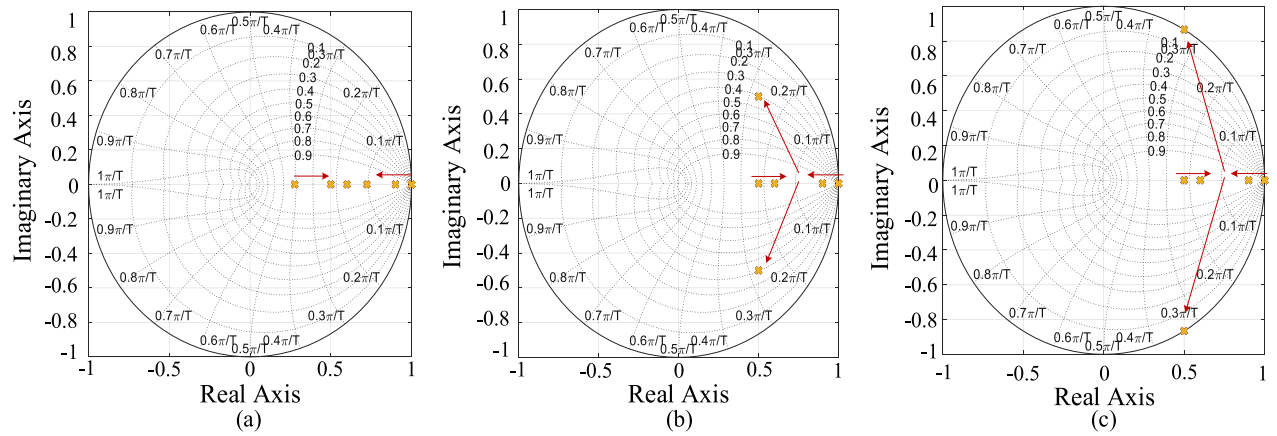

Fig. 8. Trajectories of eigenvalues against G_{p}. (a) $G_{\mathrm{p}} = 2$. (b) $G_{\mathrm{p}} = 6$. (c) $G_{\mathrm{p}} = 10$.

to the unit circle and the damping factor of the system will be smaller.

Fig. 9 summarizes the overall control of the dc cascaded system. The NI inductance is obtained by using (2). According to (18), the system parameter $w(k)$ at kth instant is calculated through V_{in}, $i_{\mathrm{NI}}(k)$, and $L_{\mathrm{NI}}(k)$. The estimations of the output voltage $V_{\mathrm{out}}(\tilde{k}+1)$, the output current $i_{\mathrm{out}}(\tilde{k}+1)$, and the system parameter $w(\tilde{k})$ are derived as per observers 1 and 2. The value of the CPL power at $(k+1)$th cycle is estimated by (28). Based on $L_{\mathrm{NI}}(k)$, NI current $i_{\mathrm{NI}}(k)$, and target NI current $i_{\mathrm{NIref}}(k)$ at the kth cycle, the proposed MPC technique outputs the duty cycle $d(k)$ or $d_{\mathrm{th}}(k)$ to generate the gate signal. The switching frequency is kept constant. The observers and the system stability are also discussed to quantitatively select the observer parameters, the sampling period, and the controller parameter in (16).

Based on the above discussion, the function of the current loop is used to determine the required duty cycle to make the NI current reach the target current i_{NIref} in one switching cycle. Equation (13) is the mathematical expression of the duty cycle, where the inductance value of the NI is determined by the formula given in (2). The function of the voltage loop is used to regulate the output voltage by deriving the value of i_{NIref} for the current loop in Section IV-B. In Section IV-C, the system

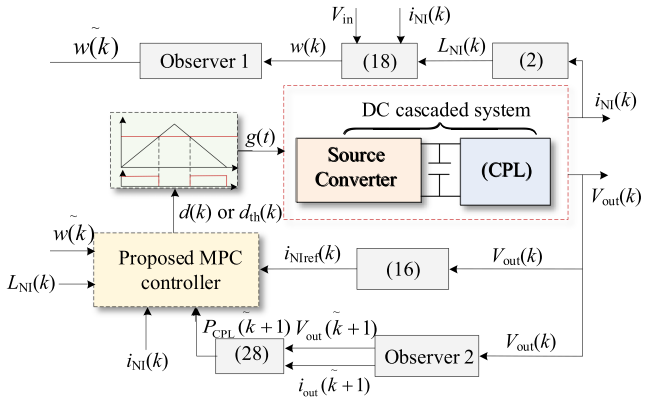

Fig. 9. Block diagram of the proposed MPC control for the entire dc cascaded system.

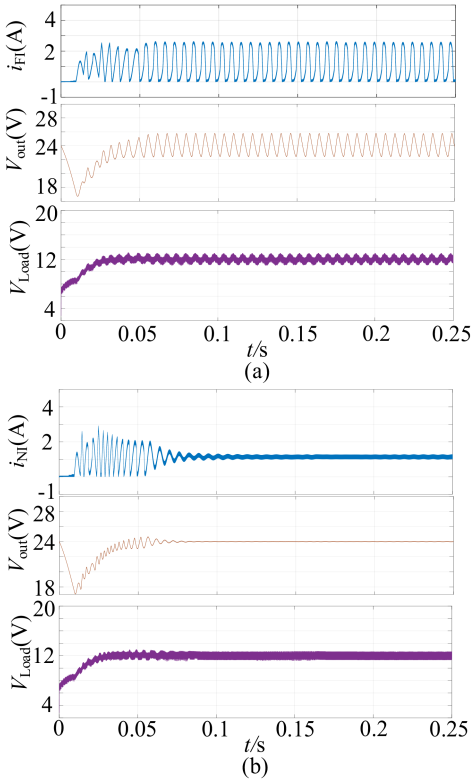

Fig. 10. Simulation results of the inductor current, output voltage, and load voltage at the power level of 12 W. (a) With FI. (b) With NI.

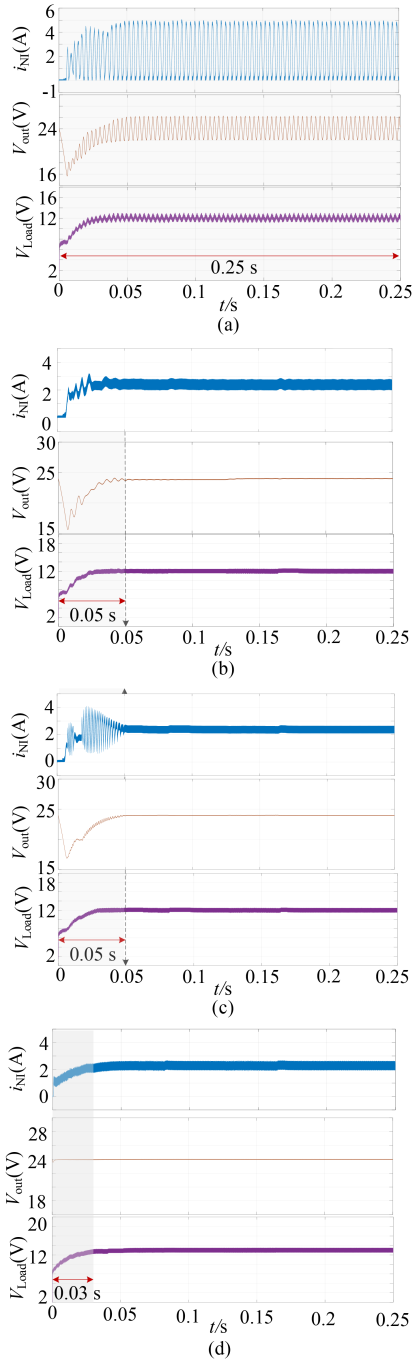

Fig. 11. Simulation results using different control techniques with NI upon an abrupt change of the power level from 0 to 24 W. (a) PI control with NI. (b) PI with the active damping technique given in [8] and NI. (c) PI with the active damping technique given in [16] and NI. (d) Proposed MPC technique with NI.

stability against the control parameters is given. Based on the comparative study in Section V hereinafter, it will be found that the NI can enhance the system stability, as compared with the system with an inductor of a fixed value.

V. Verification and Comparative Results

A. Simulation Results

To verify the effectiveness of the proposed MPC technique, a dc cascaded system is simulated on MATLAB/Simulink. The parameters used in the simulation are: $V_{\rm in} = 12$ V, $V_{\rm out} = 24$ V, $V_{\rm Load} = 12$ V, $T_{\rm s} = 20$ μs, and the switching frequency is 50 kHz. The performances with NI and FI are compared. The value of the FI is 2 mH. The NI has the same value of 2 mH when the inductor current is 0 A. Its value becomes 1.1 mH when the inductor current is 1 A.

1) Performance With PI Controller: In Fig. 10, the performance of the system is shown when the two types of inductors are used separately with a PI controller. The power level is set

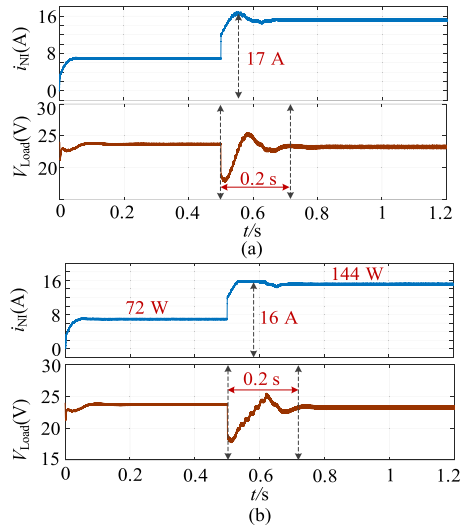

Fig. 12. NI current and the output voltage. (a) Without NI current limit. (b) With NI current limit using (12).

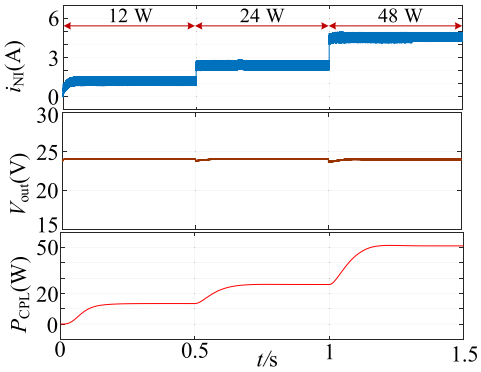

Fig. 13. Simulation results of the system performance and the observer to estimate the power of the CPL under the dynamic load changes.

at 12 W. It is observed that the NI improves the stability of the system more effectively than the FI. This demonstrates the advantages of using the NI for enhancing the stability of dc cascaded systems.

2) Comparisons of Different Control Methods With NI: The simulation results using different control methods combined with NI are shown in Fig. 11. The NI current, output voltage, and load voltage upon an abrupt change of the power level from 0 to 24 W are illustrated. Notably, the dc cascaded system is unstable when employing a PI-based control technique with NI. Low-frequency oscillations in the $i_{\rm NI}$ and $V_{\rm out}$ are observed, as shown in Fig. 11(a).

Introduction of two active damping techniques, proposed in [8] and [16], respectively, [see Fig. 11(b)–(c)] through feedforward and in feedback manners result in stable system operation compared with the conventional PI-based control techniques, accordingly with the settling time of approximately 0.05 s to reach 95% of the steady-state value. Nevertheless, some degree of ripples persists in the NI current and output voltage, due to the presence of the integral gain within these techniques. When the proposed MPC technique [see Fig. 11(d)] is applied, it not only guarantees stable operation of the entire system but also facilitates fast dynamic response. The output reaches 95% of the steady-state value after 0.03 s.

TABLE II
COMPONENT PARAMETERS FOR EXPERIMENTAL VERIFICATION

Parameters	Symbol	Value
NI inductance	$L_{\rm NI}$	2 mH
Parasitic inductor resistance	$R_{\rm NI}$	0.3 Ω
Sampling period	$T_{\rm s}$	20 μS
Output capacitance	C_1	200 μF
Quiescent duty cycle	D	0.5
The input voltage	$V_{\rm in}$	12 V
The output voltage	$V_{\rm out}$	24 V

3) Current Limit: To test the current limit function of the MPC technique given in (12), the power level of the system is changed from 72 to 144 W, intentionally exceeding the limit of the NI current. Fig. 12 shows that without the NI current limit, the proposed MPC technique surpasses the NI current by more than 17 A [see Fig. 12(a)]. However, by implementing the proposed MPC technique outlined in (12), the NI current is effectively constrained to 16 A [see Fig. 12(b)] while maintaining a transient period of approximately 0.2 s for $V_{\rm out}$. This capability is particularly advantageous for protecting the dc cascaded system during start-up and load-changing phases, where a surge in current may occur.

4) Verification of the Robustness: To verify the performance and the robustness of the observers proposed in Section IV-C, the power of the CPL is changed from 12 to 24 W, and then to 48 W, as shown in Fig. 13. The proposed observer accurately estimates $P_{\rm CPL}$ while ensuring the stable NI current and output voltage.

In Fig. 14(a), the system robustness under parameter variations is observed. The variations include 20% change in $V_{\rm in}$, $R_{\rm NI}$, C_1, and the parameter w. As depicted in Fig. 14(a), an increase in these parameters leads to a decrease in the NI current, attributed to the increased voltage across the NI. Importantly, the proposed technique ensures both steady-state operation and smooth dynamic transients. Fig. 14(b) shows the operation of the dc cascaded system under the same uncertain parameters, reduced by -20%. In this scenario, the NI current decreases as the voltage across the NI diminishes. Furthermore, the dc cascaded system exhibits stable performance in terms of both output voltage and NI current, underscoring its resilience to parameter variations, because the observers are integrated into the proposed MPC approach.

B. Experimental Results: To further verify the effectiveness of the proposed MPC technique, a small-scaled boost prototype is implemented. The setup is shown in Fig. 15. The part numbers of the components are silicon carbide (SiC) devices (SCT2120AFC), microcontroller (DSP: TMS320F28379D), power source (GPC-303OD), and point-to-load source (NID100-R1), and the oscilloscope (MDO3024). The parameters are listed in Table II.

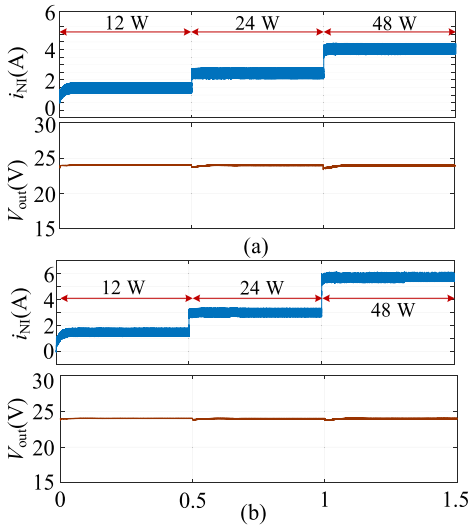

Fig. 14. Simulation results of the system performance with mismatched parameters under the dynamic load changes. (a) $\triangle w = 20\%$ of w and $\triangle C_1 = 20\%$ of C_1. and (b) $\triangle w = -20\%$ of w and $\triangle C_1 = -20\%$ of C_1.

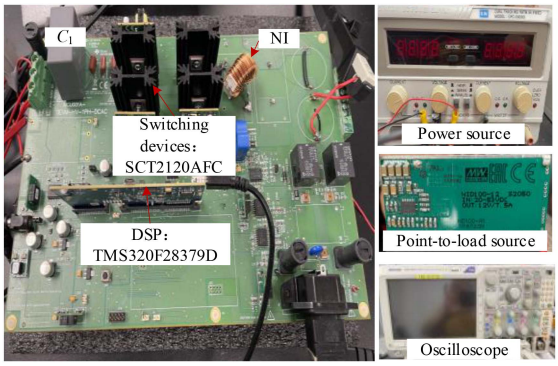

Fig. 15. Small-scaled prototype.

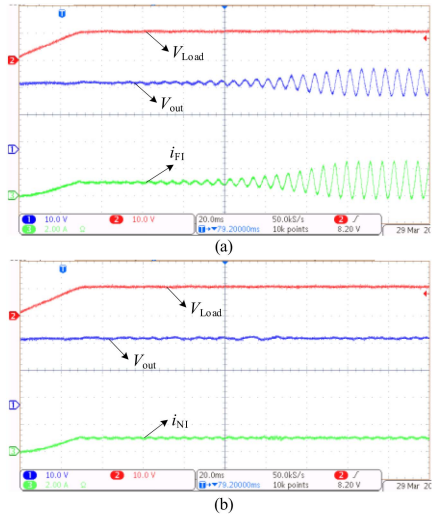

Fig. 16. Experimental results of the inductor current, output voltage, and load voltage at the power level of 12 W. (a) PI control with FI. (b) PI control with NI. (Ch1: 10V/div, Ch2, 10V/div, Ch3: 2A/div. Time base: 20ms/div.).

Fig. 16 shows the system performance using two different techniques: (PI+FI) and (PI+NI), which are also shown in Fig. 10 for the sake of comparison. The (PI+FI) technique fails to stabilize the system under this condition, whereas the (PI+NI) technique succeeds in stabilizing the system from startup to the steady state. It is worth noting that the inclusion of the NI technique once again proves its effectiveness in enhancing system stability.

The steady-state results of comparative experiments using different control techniques combined with NI are shown in Fig. 17. Corresponding with the simulation results in Fig. 11, these experimental results present the NI current, output voltage, and load voltage controlled at a power level of 16 W in a dc cascaded system, using the following:

$$\begin{bmatrix} i_{NI}(k+1) \\ V_{out}(k+1) \\ d(k+1) \\ w(k+1) \\ i_{out}(k+1) \\ i_{NI}(\tilde{k}+1) \\ V_{out}(\tilde{k}+1) \\ w(\tilde{k}+1) \\ i_{out}(\tilde{k}+1) \end{bmatrix} = \begin{bmatrix} 0 & -G_P & 0 & 0 & 0 & 0 & 0 & 0 & 0 \\ -T_s[D(k)-1]/C_1 & 1 & 0 & 0 & -T_s/C_1 & 0 & 0 & 0 & 0 \\ 0 & 0 & 1 & 0 & 0 & 0 & 0 & 0 & 0 \\ R_{NI}/L_{NI} & G_P R_{NI}/L_{NI} & 0 & 1 & 0 & 0 & 0 & 0 & 0 \\ 0 & 0 & 0 & 0 & 1 & 0 & 0 & 0 & 0 \\ O_1 & -[1-D(k)]T_s/L_{NI} & 0 & 0 & 0 & (1-O_1) & 0 & T_s & 0 \\ T_s[1-D(k)]/C & p_2 & 0 & 0 & 0 & 0 & (1-p_2) & 0 & -T_s C_1 \\ h_2 & 0 & 0 & 0 & 0 & -O_2 & 0 & 1 & 0 \\ 0 & p_1 & 0 & 0 & 0 & 0 & -p_1 & 0 & 1 \end{bmatrix}$$

$$\begin{bmatrix} i_{NI}(k) \\ V_{out}(k) \\ d(k) \\ w(k) \\ i_{out}(k) \\ i_{NI}(\tilde{k}) \\ V_{out}(\tilde{k}) \\ w(\tilde{k}) \\ i_{out}(\tilde{k}) \end{bmatrix} + \begin{bmatrix} G_P V_{outref} \\ 0 \\ 0 \\ G_I \\ 0 \\ 0 \\ 0 \\ 0 \\ 0 \end{bmatrix} \tag{32}$$

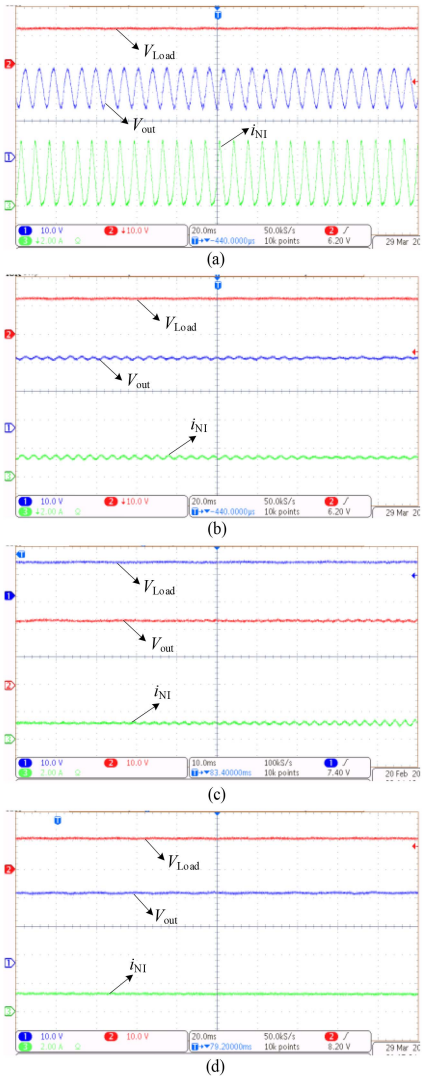

Fig. 17. Steady-state comparative experimental results of different control techniques with NI in terms of the NI current, the output voltage, and the load voltage at the power level of 16 W. (a) PI-based control technique with NI. (b) Active damping-based control technique with NI in [8]. (c) Active damping-based control technique with NI in [16]. (d) MPC-based technique with NI. (Ch1: 10V/div, Ch2, 10V/div, Ch3: 2A/div. Time base: 20 ms/div.)

1) the PI-based control technique with NI;
2) the active damping-based control techniques, proposed in [8] and [16], with NI;
3) the proposed MPC with NI.

Of these control techniques, the proposed MPC with NI demonstrates optimal stability in the dc cascaded system, with the active damping based control techniques in [8] and [16] combined with NI closely following, and the PI-based control technique with NI giving the worst performance.

Fig. 18 presents the dynamic responses of various control techniques combined with NI under a sudden load change. Both the active damping-based control techniques with NI detailed in [8] and [16], as well as the proposed technique, successfully stabilize the dc cascaded system at a power level of 12 W. However, when the power level is changed to 22 W, the system experiences a long settling time in NI current and output

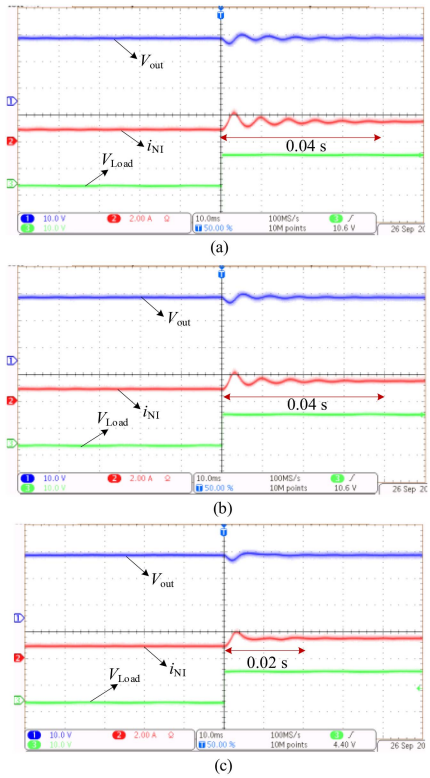

Fig. 18. Comparative dynamic responses of different control techniques with NI when the power level is changed from 12 to 22 W. (a) Active damping-based control technique with NI in [8]. (b) Active damping-based control technique with NI in [16]. (c) MPC-based technique with NI. (Ch1: 10 V/div, Ch2, 2 A/div, Ch3: 10 V/div. Time base: 10 ms/div.)

voltage when employing the techniques described in [8] and [16]. In contrast, the proposed technique continues to maintain the stability of the dc cascaded system at this increased power level, accomplishing this within an impressive 0.02 s transition period.

To experimentally verify the effectiveness and robustness of the observers proposed in Section III, an experimental test is illustrated in Fig. 19, which examines the performance of the system with variations of $\pm 20\%$ in multiple parameters including source voltage V_{in}, NI resistance R_{NI}, output capacitance C_1, and parameter w under the steady-state operation of the system. As shown in Fig. 19, when these uncertain parameters change by $\pm 20\%$, the dc cascaded system remains stable in terms of the output voltage and NI current. The experimental result indicates that the MPC technique incorporating the proposed observers ensures system stability even in the face of parameter uncertainty.

Fig. 20 experimentally investigates the system with the parameter variation under the dynamic operation of the system. With respect to Fig. 20, the system operates stably under the dynamic transition process, which demonstrates the robustness of the proposed technique.

C. Comparative Study

Table III provides a comprehensive comparison of the proposed MPC technique and state-of-the-art techniques in various

TABLE III
COMPARISON OF EXISTING AND PROPOSED TECHNIQUES

Technique	Control	Improving stability range	Switching frequency	Overcurrent protection	Study of robustness	Resources	Computing time μs	Memory usage (kB)
[10]	PI+ Passive damping	Not discussed	Fixed	Not included	No	M: 2 A: 2	0.12	12
[13]						M: 2 A: 2	0.12	12
[14]	PI+ Active damping					M:2 A:2	0.12	16
[17]			Variable			M: 3 A:3	0.18	12
[18]	MPC				Yes	M: 10 A:5 D:4	1.11	44
[24]						M: 15 A:11 D:4	1.44	72
Proposed		Discussed	Fixed	Included		M: 4 A: 7 D:1	0.495	32

*M: no. of multiplications, A: no. of additions, and D: no. of divisions.

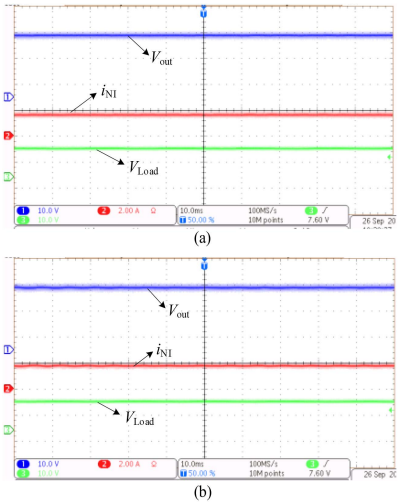

Fig. 19. Steady-state experimental results of the system performance under the parameter uncertainty condition. (a) $\triangle w = 20\%$ of w and $\triangle C_1 = 20\%$ of C_1. (b) $\triangle w = -20\%$ of w and $\triangle C_1 = -20\%$ of C_1. (Ch1: 10 V/div, Ch2, 2 A/div, Ch3: 10 V/div. Time base: 10 ms/div.)

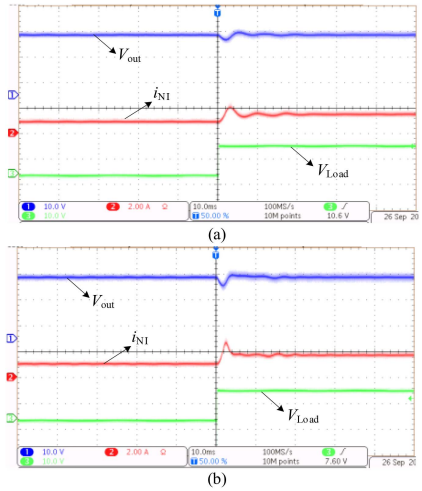

Fig. 20. Dynamic-state experimental results of the system performance under the mismatched parameters from the power level of 12 W to 22 W. (a) $\triangle w = 20\%$ of w and $\triangle C_1 = 20\%$ of C_1. (b) $\triangle w = -20\%$ of w and $\triangle C_1 = -20\%$ of C_1. (Ch1: 10 V/div, Ch2, 2 A/div, Ch3: 10 V/div. Time base: 10 ms/div.).

aspects. In terms of the control system structure, techniques in [10] and [13] use passive damping, resulting in reduced system efficiency, increased power losses, and costs. These demerits are not associated with the active damping-based and MPC techniques in [8], [16], [22], and [24], and the proposed MPC technique. In addition, the proposed MPC technique improves system stability through NI implementation, which is not presented in any of the techniques. Regarding the switching frequency, techniques in [8], [10], [13], [16], and the proposed MPC technique use a triangle wave to set the switching frequency. However, MPC techniques in [22] and [24] directly generate PWM signals, which lead to unfixed switching frequencies. In addition, the complex digital implementation caused by a long-predicted horizon in [22] and [24] is not an issue with the proposed MPC technique, which reduces the predicted horizon by using the deadbeat principle and simplifies the digital implementation. Regarding robustness, the proposed MPC technique and techniques in [22] and [24] introduce corresponding observers to ensure immunity to parameter uncertainty. To limit the rush current, the proposed MPC technique considers the NI current amplitude by the duty cycle in (12). This aspect is beneficial to the practical application.

To further emphasize the simplicity of the proposed MPC technique, a quantitative comparison of the controllers themselves is presented by focusing on the digital resources, the computing time, and the memory usage. The PI controllers in [8], [10], [13], and [16] require fewer multiplication, addition, and division operations, accordingly resulting in less computing

time and memory usage consumption. The MPC controllers in [22] and [24] need to enumerate the optimized state and conduct the derivative operation so that more digital resources are required than the proposed controller, which applies the dead-beat principle to reduce the prediction horizon.

VI. Conclusion and Discussions

This article introduces a novel approach that combines MPC with the utilization of NIs in the PCS to enhance the stability of dc cascaded systems with CPLs. The proposed technique offers the following advantages.

1) Simplified implementation of MPC based on the deadbeat principle, resulting in a reduced predictive horizon and digital implementation complexity.
2) Expanded stability range of the control-to-output transfer characteristics.
3) Improved steady-state and faster dynamic performance.
4) Inherent current limit capability within the MPC technique eliminates the need for external hardware protection circuits, making it more practical for real-world applications.
5) Development of two observers to enhance system robustness in the presence of parameter uncertainties. Guidelines for quantizing the observer parameters to ensure stability are provided, aiding in parameter selection.

The stability of the overall system is studied to determine the controller parameters. A power electronic system typically consists of two main components: PCS and the controller. Popular impedance-based stability improvement methods primarily focus on developing advanced control schemes to address the interaction between the PCS and CPL, without modifying the PCS structure. In contrast, our approach aims to enhance the stability of the PCS with CPL by first improving the open-loop operation from the control signal to the output. The utilization of NIs can broaden the stability range of the control-to-output transfer characteristics. Subsequently, an MPC technique is proposed to enhance the overall performance of the dc cascaded system.

The key impact of the use of NI is that the current ripple increases as P_{CPL} increases. This is attributed to the fact that the NI experiences a reduction in its inductance as its current rises. However, it is important to note that, as long as, the current ripple remains within an acceptable percentage, no detrimental effects are observed.

Further research will be dedicated to applying NI to other types of converters and enhancement of complex dc microgrids that involve multiple voltage sources and loads.

References

[1] A. Kwasinski and C. N. Onwuchekwa, "Dynamic behavior and stabilization of DC microgrids with instantaneous constant-power loads," *IEEE Trans. Power Electron.*, vol. 26, no. 3, pp. 822–834, Mar. 2011.

[2] E. Hossain, R. Perez, A. Nasiri, and S. Padmanaban, "A comprehensive review on constant power loads compensation techniques," *IEEE Access*, vol. 6, pp. 33285–33305, 2018.

[3] S. Singh, A. R. Gautam, and D. Fulwani, "Constant power loads and their effects in DC distributed power system: A review," *Renewable Sustain. Energy Rev.*, vol. 72, pp. 407–421, 2017.

[4] R. Shen and H. S.-H. Chung, "On the use of nonlinear inductor to enhance the stability of dc distribution networks," *IEEE Trans. Power Electron.*, vol. 37, no. 7, pp. 8582–8595, Jul. 2022.

[5] N. Sarrafan et al., "A novel fast fixed-time backstepping control of dc microgrids feeding constant power loads," *IEEE Trans. Ind. Electron.*, vol. 70, no. 6, pp. 5917–5926, Jun. 2023.

[6] M. Zhang, Y. Li, F. Liu, L. Luo, Y. Cao, and M. Shahidehpour, "Voltage stability analysis and sliding-mode control method for rectifier in dc systems with constant power loads," *IEEE J. Emerg. Sel. Topics Power Electron.*, vol. 5, no. 4, pp. 1621–1630, Dec. 2017.

[7] R. Shen and H. S.-H. Chung, "Mitigation of ground leakage current of single-phase PV inverter using hybrid PWM with soft voltage transition and nonlinear output inductor," *IEEE Trans. Power Electron.*, vol. 36, no. 3, pp. 2932–2946, Mar. 2021.

[8] A. M. Rahimi and A. Emadi, "Active damping in dc/dc power electronic converters: A novel method to overcome the problems of constant power loads," *IEEE Trans. Ind. Electron.*, vol. 56, no. 5, pp. 1428–1439, May 2009.

[9] K. E. Lucas et al., "Robust control of interconnected power electronic converters to enhance performance in dc distribution systems: A case of study," *IEEE Trans. Power Electron.*, vol. 36, no. 4, pp. 4851–4863, Apr. 2021.

[10] A. Khaligh, "Realization of parasitics in stability of dc–dc converters loaded by constant power loads in advanced multiconverter automotive systems," *IEEE Trans. Ind. Electron.*, vol. 55, no. 6, pp. 2295–2305, Jun. 2008.

[11] M. Wu and D. D.-C. Lu, "A novel stabilization method of *LC* input filter with constant power loads without load performance compromise in dc microgrids," *IEEE Trans. Ind. Electron.*, vol. 62, no. 7, pp. 4552–4562, Jul. 2015.

[12] M. A. Hassan, E.-P. Li, X. Li, T. Li, C. Duan, and S. Chi, "Adaptive passivity-based control of dc–dc buck power converter with constant power load in dc microgrid systems," *IEEE J. Emerg. Sel. Topics Power Electron.*, vol. 7, no. 3, pp. 2029–2040, Sep. 2019.

[13] M. Cespedes, L. Xing, and J. Sun, "Constant-power load system stabilization by passive damping," *IEEE Trans. Power Electron.*, vol. 26, no. 7, pp. 1832–1836, Jul. 2011.

[14] K. A. Potty, E. Bauer, H. Li, and J. Wang, "Smart resistor: Stabilization of dc microgrids containing constant power loads using high-bandwidth power converters and energy storage," *IEEE Trans. Power Electron.*, vol. 35, no. 1, pp. 957–967, Jan. 2020.

[15] B. He, W. Chen, X. Li, L. Shu, and X. Ruan, "A power adaptive impedance reshaping strategy for cascaded dc system with buck-type constant power load," *IEEE Trans. Power Electron.*, vol. 37, no. 8, pp. 8909–8920, Aug. 2022.

[16] Y. Li, P. Y. Jia, and T. Q. Zheng, "Active damping method to reduce the output impedance of the dc–dc converters," *IET Power Electron.*, vol. 8, no. 1, pp. 88–95, 2015.

[17] A. Hosseinipour and H. Hojabri, "Small-signal stability analysis and active damping control of dc microgrids integrated with distributed electric springs," *IEEE Trans. Smart Grid*, vol. 11, no. 5, pp. 3737–3747, Sep. 2020.

[18] G. Sulligoi, D. Bosich, G. Giadrossi, L. Zhu, M. Cupelli, and A. Monti, "Multiconverter medium voltage dc power systems on ships: Constant-power loads instability solution using linearization via state feedback control," *IEEE Trans. Smart Grid*, vol. 5, no. 5, pp. 2543–2552, Sep. 2014.

[19] B. Babaiahgari, Y. Jeong, and J.-D. Park, "Dynamic control of region of attraction using variable inductor for stabilizing dc microgrids with constant power loads," *IEEE Trans. Ind. Electron.*, vol. 68, no. 10, pp. 10218–10228, Oct. 2021.

[20] M. Mosayebi, S. M. Sadeghzadeh, M. Gheisarnejad, and M. H. Khooban, "Intelligent and fast model-free sliding mode control for shipboard dc microgrids," *IEEE Trans. Transp. Electrific.*, vol. 7, no. 3, pp. 1662–1671, Sep. 2021.

[21] W. He and R. Ortega, "Design and implementation of adaptive energy shaping control for dc–dc converters with constant power loads," *IEEE Trans. Ind. Inform.*, vol. 16, no. 8, pp. 5053–5064, Aug. 2020.

[22] Q. Xu, C. Zhang, C. Wen, and P. Wang, "A novel composite nonlinear controller for stabilization of constant power load in dc microgrid," *IEEE Trans. Smart Grid*, vol. 10, no. 1, pp. 752–761, Jan. 2019.

[23] J. Chen et al., "Power flow control-based regenerative braking energy utilization in ac electrified railways: Review and future trends," *IEEE Trans. Intell. Transp. Syst.*, to be published, doi: 10.1109/TITS.2024.3350743.

[24] Q. Xu, Y. Yan, C. Zhang, T. Dragicevic, and F. Blaabjerg, "An offset-free composite model predictive control strategy for dc/dc buck converter feeding constant power loads," *IEEE Trans. Power Electron.*, vol. 35, no. 5, pp. 5331–5342, May 2020.
[25] P. Karamanakos, T. Geyer, and S. Manias, "Direct model predictive current control strategy of dc–dc boost converters," *IEEE J. Emerg. Sel. Topics Power Electron.*, vol. 1, no. 4, pp. 337–346, Dec. 2013.
[26] P. Karamanakos, T. Geyer, and S. Manias, "Direct voltage control of dc–dc boost converters using enumeration-based model predictive control," *IEEE Trans. Power Electron.*, vol. 29, no. 2, pp. 968–978, Feb. 2014.
[27] Y. Xiang, H. S.-H. Chung, and H. Lin, "Light implementation scheme of ANN-based explicit model-predictive control for dc-dc power converters," *IEEE Trans. Ind. Inform.*, to be published, doi: 10.1109/TII.2023.3319654.
[28] H. Lin, S. Niu, Z. Xue, and S. Wang, "A simplified virtual-vector-based model predictive control technique with a control factor for three-phase SPMSM drives," *IEEE Trans. Power Electron.*, vol. 38, no. 6, pp. 7546–7557, Jun. 2023.
[29] D. Xie, C. Lin, H. Lin, W. Liu, Y. Du, and T. Basler, "OC switch fault diagnosis, pre- and postfault dc voltage balancing control for a CHBMC using SVM concept," *IEEE Trans. Power Electron.*, vol. 39, no. 1, pp. 677–692, Jan. 2024.
[30] J. Chen et al., "Analysis and control of cascaded energy storage system for energy efficiency and power quality improvement in electrified railways," *IEEE Trans. Transp. Electrific.*, to be published, doi: 10.1109/TTE.2023.3287891.
[31] Y. Zuo et al., "A novel current measurement offset error compensation method based on the adaptive extended state observer for IPMSM drives," *IEEE Trans. Ind. Electron.*, vol. 71, no. 4, pp. 3371–3382, Apr. 2024.
[32] Y. Zuo, H. Wang, X. Ge, J. Mu, C. Lin, and C. H. T. Lee, "A novel single-phase current sensor control strategy based on dual APF-QSG for position-sensorless IPMSM drives," *IEEE Trans. Power Electron.*, vol. 39, no. 1, pp. 71–77, Jan. 2024, doi: 10.1109/TPEL.2023.3323408.
[33] J. Zhao, C. Xie, K. Li, J. Zou, and J. M. Guerrero, "Passivity-oriented design of *LCL*-type grid-connected inverters with Luenberger observer-based active damping," *IEEE Trans. Power Electron.*, vol. 37, no. 3, pp. 2625–2635, Mar. 2022.

Hongjian Lin (Senior Member, IEEE) received the Ph.D. degree in electrical engineering from Southwest Jiaotong University, Chengdu, China, in 2021.

From 2019 to 2020, he was a visiting researcher with the School of Electrical and Computer Engineering, Georgia Institute of Technology, Atlanta, GA, USA. From 2021 to 2022, he was a postdoctoral research associate with the Department of Electrical Engineering, Hong Kong Polytechnic University, Hong Kong. He is currently a postdoctoral research fellow with the Department of Electrical Engineering, City University of Hong Kong, Hong Kong. His research interests include nonlinear and artificial intelligence control of dc–dc converters in microgrids, electromagnetic materials property analysis, electrical machines and drives control, wireless power transfer techniques, and modulation and control techniques of multilevel converters in the solid-state transformer.

Dr. Lin is a Guest Associate Editor for IEEE TRANSACTIONS ON POWER ELECTRONICS.

Henry Shu-Hung Chung (Fellow, IEEE) received the B.Eng. and Ph.D. degrees in electrical engineering from Hong Kong Polytechnic University, Hong Kong, in 1991 and 1994, respectively.

Since 1995, he has been with the City University of Hong Kong, Hong Kong, where he is currently the Dean of Students, a Chair Professor with the Department of Electrical Engineering, and the Director of the Centre for Smart Energy Conversion and Utilization Research. He has authored one book, eight research book chapters, and more than 500 technical papers including 250 refereed journal papers in his research areas, and holds 80 patents. His research interests include renewable energy conversion technologies, lighting technologies, energy harvesting, smart grid technologies, and computational intelligence for power electronic systems.

Dr. Chung is currently an Associate Editor for IEEE TRANSACTIONS ON POWER ELECTRONICS and IEEE JOURNAL OF EMERGING AND SELECTED TOPICS IN POWER ELECTRONICS. From 2014 to 2018, he was Editor-in-Chief of the IEEE POWER ELECTRONICS LETTERS. From 2010 to 2014, he was also the Chair of the Technical Committee of the High-Performance and Emerging Technologies, IEEE Power Electronics Society. He was the recipient of the 2021 IEEE PELS R. David Middlebrook Achievement Award, the CityU Outstanding Research Award in 2020, and the CityU Teaching Excellence Awards in 2018 and 2022. He was also the recipient of numerous industrial awards for his invented energy-saving technologies.

Ruihua Shen (Member, IEEE) received the B.Eng. degree in electrical engineering from Shandong University, Jinan, China, in 2017, and the Ph.D. degree in electrical engineering from City University of Hong Kong, Hong Kong, in 2022.

She is currently with the BYD Company Ltd., Shenzhen, China. Her research interests include power conversion, dc distribution networks, and EV chargers.

Yangxiao Xiang (Member, IEEE) received the B.S. degree in electrical engineering and automation from Sichuan University, Chengdu, China, in 2014, and the Ph.D. degree in electrical engineering from Huazhong University of Science and Technology, Wuhan, China, in 2020.

He is currently a postdoctoral researcher with the Department of Electrical Engineering, City University of Hong Kong, Hong Kong. His current research focuses on the application of artificial intelligence in power electronics.